Electronic Supplementary Material (ESI) for Journal of Materials Chemistry A.

$C\text{-}O^{-}\text{-}K^{+}$ (Na^{+}) groups in non-doped carbon as active sites for oxygen reduction reaction

(Supporting Information)

Yunjie Zhou,[a §] Yue Sun,[a §] Cheng Zhu,[a] Yang Liu,[a] Xing Dai,[c] Jun Zhong,[a] Qiongyang Chen,[b] He Tian,*[b] Ruhong Zhou*[c d] and Zhenhui Kang *[a]

[a] Jiangsu Key Laboratory for Carbon-based Functional Materials and Devices, Institute of Functional Nano and Soft Materials (FUNSOM), Soochow University, Suzhou 215123, Jiangsu, China.
[b] Center of Electron Microscopy and State Key Laboratory of Silicon Materials, School of Materials Science and Engineering, Zhejiang University, Hangzhou 310027, Zhejiang, China.
[c] School for Radiological and Interdisciplinary Sciences (RAD-X), Collaborative Innovation Center of Radiological Medicine of Jiangsu Higher Education Institutions, Soochow University, Suzhou 215123, Jiangsu, China.
[d] Department of Chemistry, Columbia University, New York, NY 10027, USA.
[§] These authors contributed equally to this work.

This PDF file includes:

1. Electrochemical Measurements.

1.1 Calculation of electron transfer number (n).

Based on the RDE datas, the numbers of electron transferred per oxygen molecule could be determined by the Koutechy-Levich equation[1,2]:

$$1/j = 1/j_k + 1/B\omega^{1/2} \qquad (1)$$

In which j_k is the measured current density, and ω is the rotation speed of electrode with rpm. B is determined from the slope of the Koutechy-Levich (K-L) plots according to the Levich equation as given by[3]:

$$B = 0.2nFD_{o2}^{2/3}\upsilon^{-1/6}C_{o2} \qquad (2)$$

where n represents the electron transferred number for ORR, F is the Faraday constant (F = 96,485 C· mol^{-1}), D is the diffusion coefficient of O_2 in the 0.1 M KOH solution (D_{O2} = 1.9×10^{-5} cm^2· s^{-1}), υ is the kinetic viscosity in 0.1 M KOH solution (υ=0.01 cm^2· s^{-1}), C is the bulk concentration of O_2 in the 0.1 M KOH solution (C_{O2} = 1.2×10-6 mol· cm^{-3}), and the constant 0.2 is adopted when the rotation speed is expressed at rpm. The K–L plots obtained at different potentials of 0.3, 0.4, 0.5, 0.6 and 0.7 V.

For the RRDE measurements, electrodes were prepared by the same method as for RDE. The disk electrode was scanned at a rate of 10 mV/s, and the ring potential was constant at 1.6 V.

$$n = 4Id/(Id + Ir/N) \qquad (3)$$

where Id is disk current, Ir is ring current, and N = 0.43 is the current collection efficiency of the Pt ring.

1.2 Test of Electrochemically Active Surface Area.

The electrochemically active surface area (ECSA) for each system was estimated from the electrochemical double-layer capacitance of the catalytic surface. The electrochemical capacitance was determined by measuring the non-Faradaic capacitive current associated with double-layer charging from the scan-rate dependence of cyclic voltammograms (CVs). To measure double-layer charging via CV, a potential range in which no apparent Faradaic processes occur was determined from static CV. The range is typically a 0.1 V potential window centered at the open-circuit potential (OCP) of the system. The charging current, iC, is then measured from CVs at different scan rates. The double-layer charging current is equal to the product of the scan rate, ν, and the electrochemical double-layer capacitance, C_{DL}, as given by equation[4–6]:

$$iC = \nu\, C_{DL} \qquad (4)$$

Thus, a plot of ic as a function of ν yields a straight line with a slope equal to C_{DL}. The ECSA of a catalyst sample is calculated from the double layer capacitance according to equation:

$$ECSA = C_{DL}/Cs \qquad (5)$$

where Cs is the specific capacitance of the sample or the capacitance of an atomically smooth planar surface of the material per unit area under identical electrolyte conditions. [7] For our

estimates of surface area, we use general specific capacitances of Cs = 0.022 mF cm^{-2} in 5 M KOH based on typical reported values [7]. The CDL is 0.28175 mF in average as shown in Fig. S15

The electrochemically active surface area (ECSA) of 20%Pt/C was alculated by measuring the charge collected in the Hupd adsorption/desorption region after double-layer correction and assuming a value of 210 mC/cm^2 for the adsorption of a hydrogen monolayer (Fig. S16).

1.3 Test of electrocatalytic signal of HOPG.

The HOPG was fixed on the ITO (1.2 cm * 6.0 cm) by adhesive tape, and the treated side of HOPG is outwards. All the ITO in the electrolyte is covered with adhesive tape, keeping the ITO from the electrolyte to avoid the influence of ITO during the testing process. Other electrochemical testing processes are consistent with the main text.

2. DFT simulations:

2.1 DFT calculations for the proton donation capacities connecting hydroxyl groups of different kinds of carbon.

It can be expected that the proton donation capacity (pKa value) of the hydroxyl group on CDs-1000 is directly related to its connecting carbon atom, since different carbon species generally give rise to different charge polarizations between C and O and thus affect the binding abilities between O and H. Herein, we considered six different carbon species, including the primary sp-, sp^2-, and sp^3- carbon, the secondary sp^2(1+2)-, sp^2(π)-carbon, and the tertiary sp^3-carbon, to investigate and compare the proton donation capacities of their connecting hydroxyl groups by DFT calculations. For these six designed carbon-OH computational models, as shown in Fig. S25, a hypothetical proton dissociation reaction was assumed as

$$\text{Carbon-OH} + H_2O \rightarrow \text{Carbon-}O^- + H_3O^+ \qquad (6)$$

Geometry structures of each reactant and product of the reaction have been fully optimized at B3LYP[8,9]/6-31G*[10] level in gas phase. Single-point energies were then performed based on each optimized reactant and product at different theory of level for calculating different terms in Gibbs free energy changes (ΔG).The values of ΔG were calculated by:

$$\Delta G = \sum_{\text{product}}^{i} G - \sum_{\text{reactant}}^{i} G \qquad (7)$$

$$G = \varepsilon_{ele} + \Delta G^{sov} + E^0 + (H - TS) + 1.89\ \text{kcal/mol}\ (T = 298.15\ K) \qquad (8)$$

$$\Delta G^{sov} = E^{sol} - E^{gas} \qquad (9)$$

Where, εele is the high-precision electronic energy calculated at B2PLYP[11]/ def2TZVP[12] level; ΔGsov is the solvation energy calculated at M05-2X[13]/6-31G* level; Esol and Egas are single-point energies in liquid phase and gas phase, respectively. For calculating Esol, the implicit solvent model, SMD[14], was used with water as the solvent. E0 is the zero-point energy calculated at B3LYP/6-31G* level, which is consistent with the level of geometry optimizations. H-TS is a correction term to the Gibbs free energy (G) which were also calculated at B3LYP/6-31G* level in gas phase. H, T and S indicate the enthalpy, temperature and entropy. The 1.89 kcal/mol is a constant energy value, represen ting a 1 atm $\rightarrow$ 1 mol free energy change

from gas phase to liquid phase. All calculations in this section were performed in Gaussian 09 program.[15]

2.2 Computational models, methods and results for CD-K, CD-Na.

According to the experimental observations, we constructed two ideal alkalis-containing carbon dots (CD-K and CD-Na) as the catalyst models for theoretical simulations, as shown in Fig. S29A. In this model, a periodic (a=17.04 Å, b=22.14 Å, c=30 Å; α=β=γ=90°) defective monolayer graphene (containing 122 carbon atoms) was used as the support. The dangling carbons were saturated by 6 H atoms, 4 OH groups and 2 O^- atoms. The two O^- atoms were aimed to mimic two deprotonated OH groups. Two alkali metal ions (K^+ or Na^+) were bond onto the OH groups and the deprotonated OH groups. The CD-K and CD-Na models were then used as the adsorbents for oxygen adsorption.

As comparisons, we also constructed a Pt(111) surface model for simulating oxygen adsorption. The periodic Pt(111) model (a=b=11.10 Å, c=36.80 Å; α=β=90°, γ=120°) contains four layers Pt atoms (64 Pt atoms in total), as shown in Fig. S29B.

First principle density functional theory (DFT) calculations were performed using Dmol3 program[16,17]. The geometry structures of O_2@CD-K, O_2@CD-Na and O_2@Pt(111) models were optimized. For O_2@CD-K and O_2@CD-Na, the peripheral 88 carbon atoms were freeze and the central 34 carbon atoms, 8 H atoms, 4 OH groups, 2 O atoms, 2 K/Na ions and the adsorbing O_2 molecules were allowed to relax. For O_2@Pt(111), all Pt atoms were freeze and the adsorbing O_2 molecule was allowed to relax. The lattices of all systems were not optimized. Besides, the isolated O_2 molecule was also optimized in each different periodic box.

All geometry optimizations were carried out at PBE-D/DNP level.[18] For The O_2@CD-K, O_2@CD-Na, the all electron basis set was used. For O_2@Pt(111), the DFT-semi core pseudopots (DSPP) approach was used as the core treatment to reduce the computational consume. This approach can also introduce some degree of relativistic correction into the core. Dispertion effect was considered by introducing the Grimme scheme dispersion correction.[19] The conductor-like screening model (COSMO)[20,21] was used to simulate a solvent environment for the calculation. Other parameter settings in geometry optimizations were listed in Table S4.

The optimized O_2@CD-K, O_2@CD-Na and O_2@Pt(111) geometry structures are illustrate in Fig. S30. The relevant geometric parameters are summarized in Table S5.

After geometry optimizations, single-point energy calculations were performed for each model at PBE-D/DNP level. However, other computational parameters, including the SCF, k-points and cutoff, were set to more accurate levels, as listed in Table S6.

The energy calculation results are summarized in Table S7. For O_2@CD-K, O_2@CD-Na and O_2@Pt(111), the adsorption energies (EA) of O_2 were calculated by:

$$EA = E(\text{complex}) - E(\text{adsorbent}) - E(O_2) \qquad (10)$$

Based on energy calculations, population analyses were performed and the results are summarized in Table S8.

2.3 DFT simulations for catalytic activity of pure graphite layers with rotations.

As we found graphite layers with rotations in our CDs-1000, we also examined the effect of the rotations on the oxygen adsorption by DFT calculations. We considered three models as the adsorbents for oxygen, including single-layer graphene (SLG, containing 50 carbon atoms; α=β=90°, γ=120°; a=b=12.300 Å, c=35 Å), bi-layer AB stacking graphene (BLG, containing 100 carbon atoms; α=β=90°, γ=120°; a=b=12.300 Å, c=35 Å) and twist bi-layer graphene (tBLG, containing 112 carbon atoms, twist angle = 21.787°; α=β=90°, γ=120°; a=b=13.018 Å, c=35 Å). Geometry optimizations were carried out at PBE-D/DNP level. The conductor-like screening model (COSMO) was used to simulate a solvent environment for the calculation. Other parameter settings in geometry optimizations were listed in Table S9.

The optimized structures of O_2 adsorbing on these three models are shown in Fig. S31 and the geometric parameters are listed in Table S10. It can be seen that, for all the O_2@SLG, O_2@BLG and O_2@tBLG, the equilibrium distances between O_2 and graphene sheets are about 3 Å, suggest relatively weak physisorption characteristics. The calculated equilibrium distances in this work are well agreed with the previous DFT study (also about 3 Å, DOI: 10.1063/1.1536636). In comparison to the free O_2 molecule (with a O-O bond length of about 1.224 Å), all the SLG, BLG and tBLG adsorbents could only slightly elongate the O-O distance by about 0.02 Å.

After geometry optimizations, more accurate single-point energy calculations were performed for O_2@SLG, O_2@BLG and O_2@tBLG models at PBE-D/DNP level. The detailed computational parameters, including the SCF, k-points and cutoff, were listed in Table S11.

Based on energy calculations, we carried out the adsorption energies of O_2 mulecules adsorbing on these three adsorbents and the charge populations on oxegen atoms (Table S11). We can see that the adsorption energies of O_2 mulecules adsorbing on these three adsorbents are all about -3 kcal/mol. Each oxygen atom only takes a little negative charge (about -0.04).

From our analyses of adsorption energies, charge distributions and O-O equilibrium distances, it can be clearly seen that our K^+/Na^+-containing CDs-1000 have absolute predominance for adsorbing and decomposing O_2 molecules than the three pure carbon models. Therefore, we can conclude that the rotation effect between graphene layers is not the critical factor in enhancing ORR catalytic performance.

3. Figures

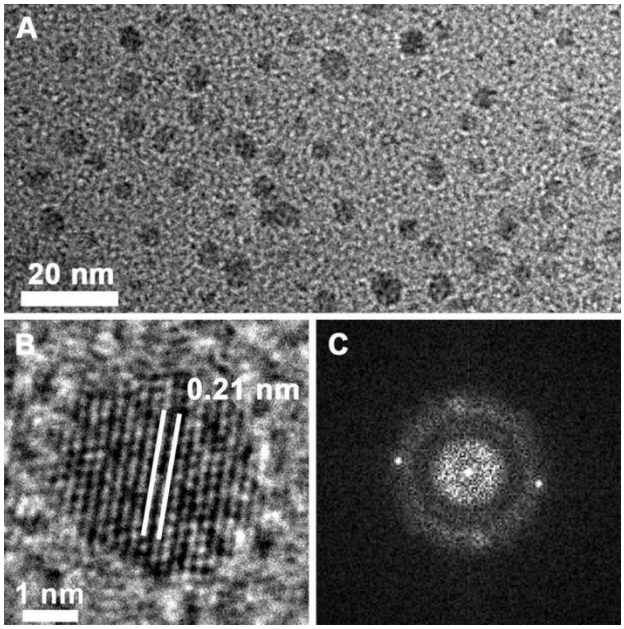

Fig. S1 Morphology of the CDs. (A) TEM image of mono-dispersed CDs. (B) HRTEM image of a single CD, and (C) corresponding FFT image of a single CD.

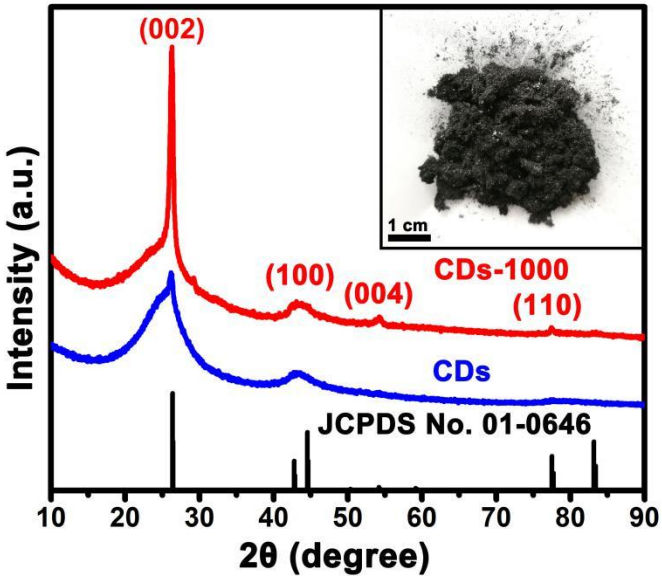

Fig. S2 Powder XRD patterns of CDs-1000 (red line), CDs (blue line), and standard card (JCPDS NO.01-0646, black line). Inset in figure: Digital photo image of CDs-1000. The CDs-1000 are black fluffy powers.

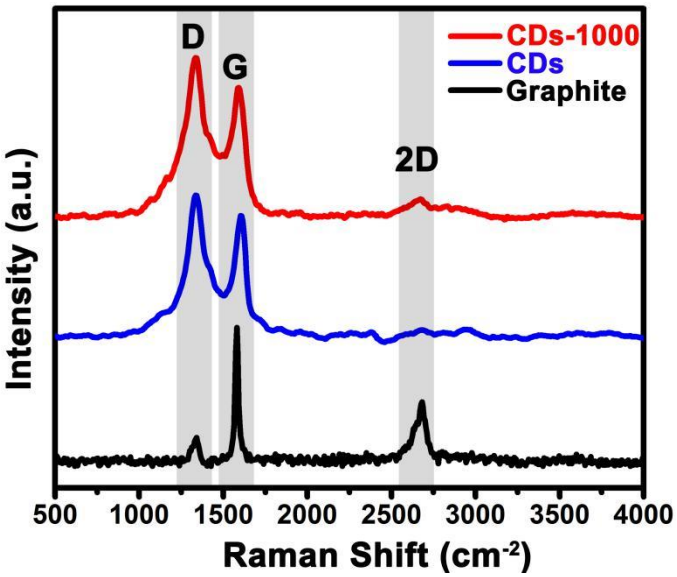

Fig. S3 Raman spectra of CDs (red line), CDs-1000 (blue line) and graphite (black line).

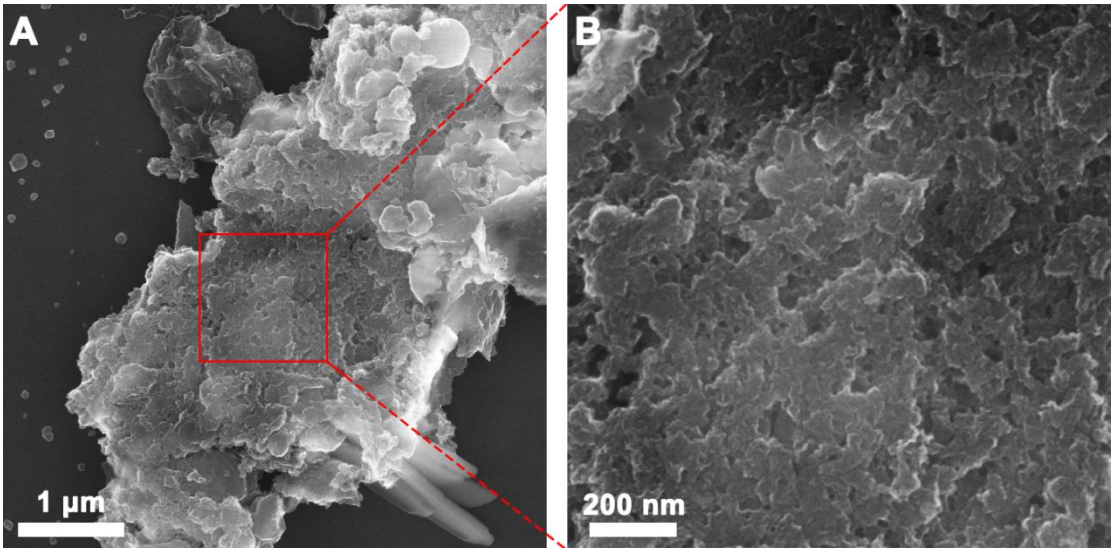

Fig. S4 (A) SEM image of CDs-1000. (B) SEM image at higher magnification of CDs-1000.

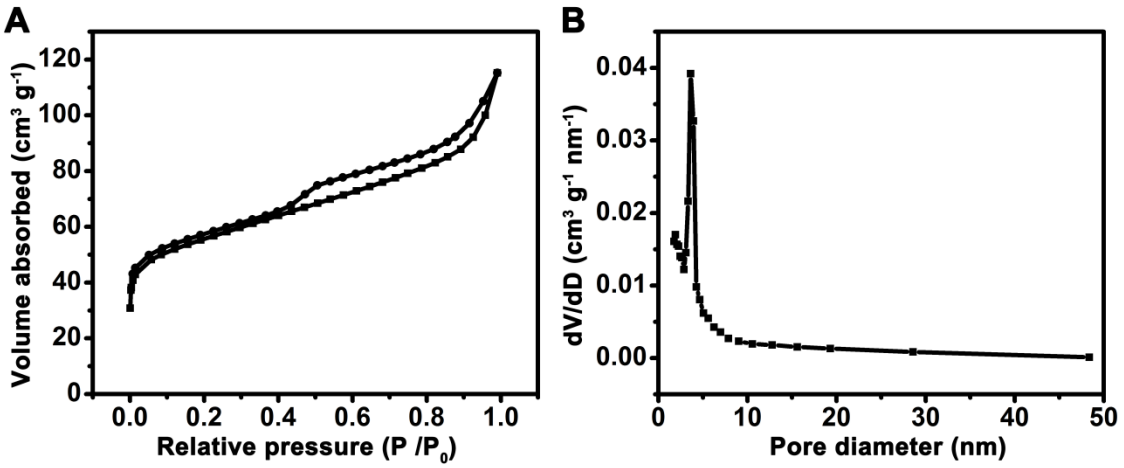

Fig. S5 Brunauer-Emmett-Teller characterization of CDs-1000. (A) N_2 adsorption-desorption isotherms. (B) Pore size distributions.

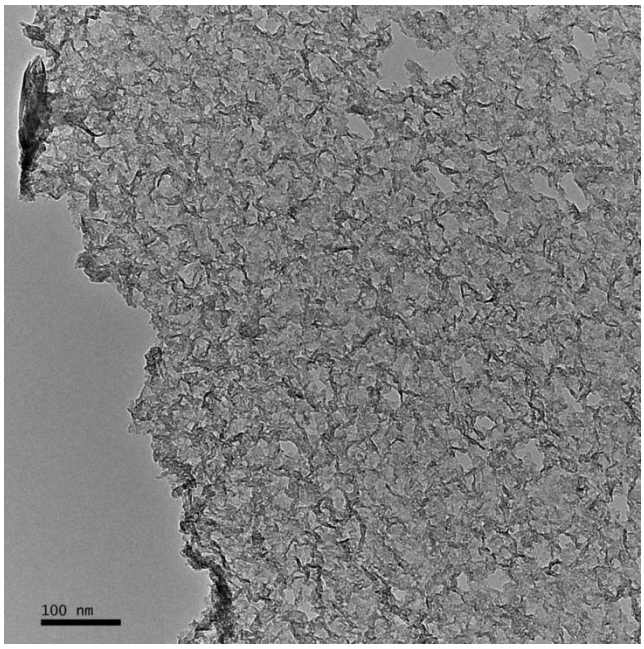

Fig. S6 TEM image of CDs-1000.

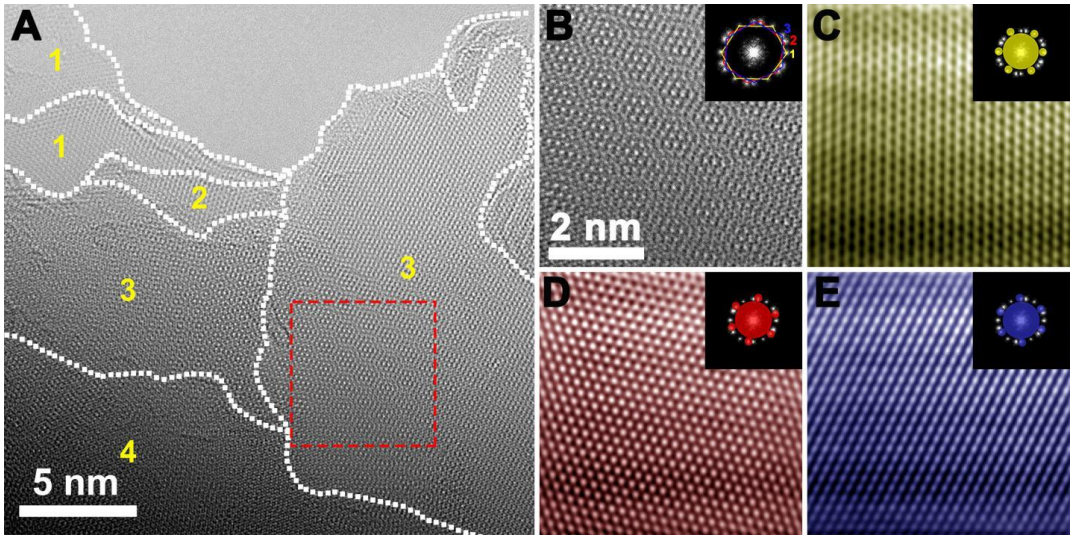

Fig. S7 (A) HRTEM image of CDs-1000. (B) Reconstructed image of the region indicated with the red box in A after filtering in the frequency domain. Inset in B is Fast Fourier transform showing three sets of hexagons with the 20˚ and 30˚ relative rotations of the three lattice orientations (versus the number one). (C-E) Reconstructed images showing the graphite layer with one set of hexagon spots removed by filtering in the frequency domain.

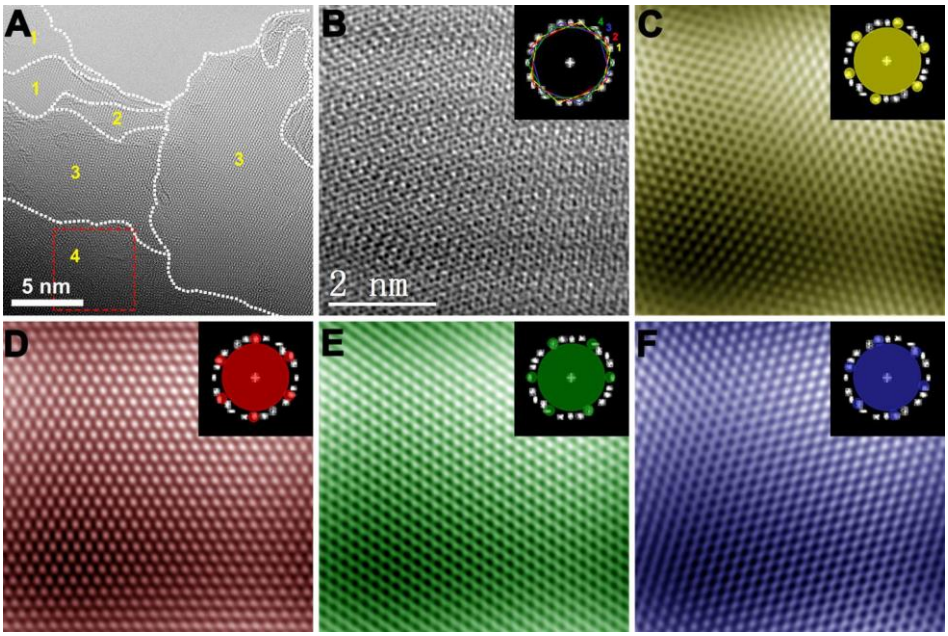

Fig. S8 (A) HRTEM image of CDs-1000. (B) Reconstructed image of the region indicated with the red box in A after filtering in the frequency domain. Inset in B is Fast Fourier transform showing four sets of hexagons with the 11˚, 24˚ and 34˚ relative rotations of the four lattice orientations (versus the number one) (C-F) Reconstructed images showing the graphite layer with one set of hexagon spots removed by filtering in the frequency domain.

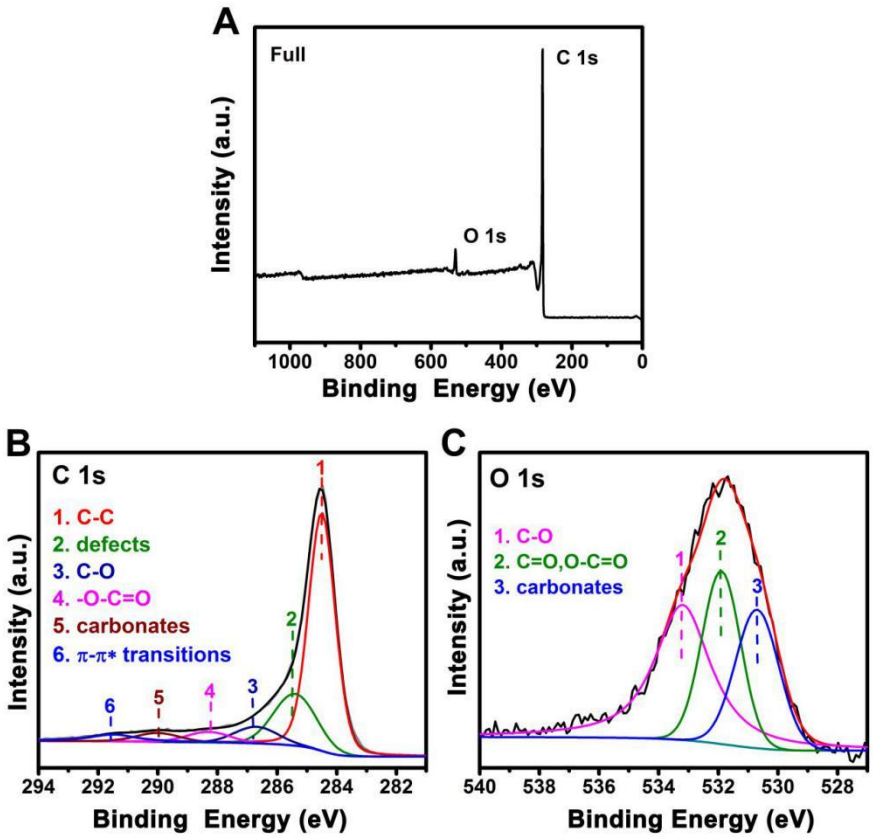

Fig. S9 (A) XPS survey spectrum of CDs-1000. The High-resolution XPS spectra of C1s (B), O1s (C) for CDs-1000.

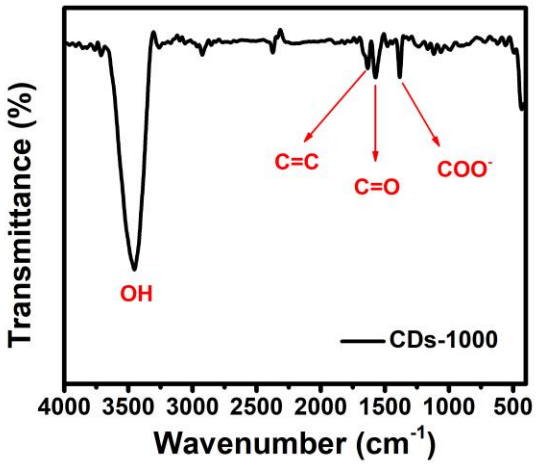

Fig. S10 FT-IR spectrum of CDs-1000.

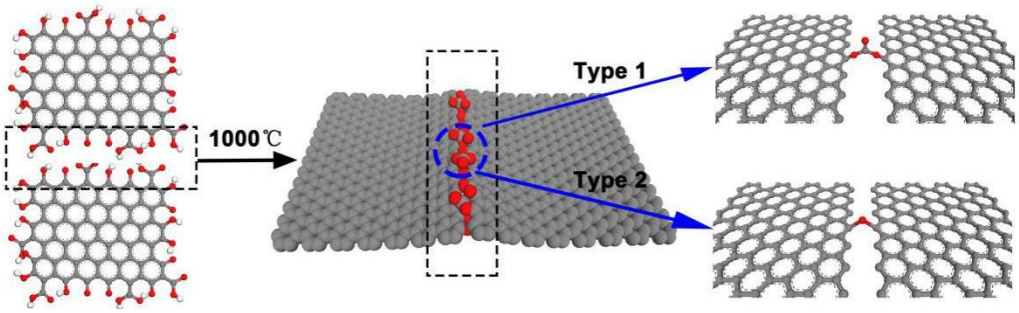

Fig. S11 Schematic diagram of synthesis of CDs-1000, and two types of connection between CDs by oxygen.

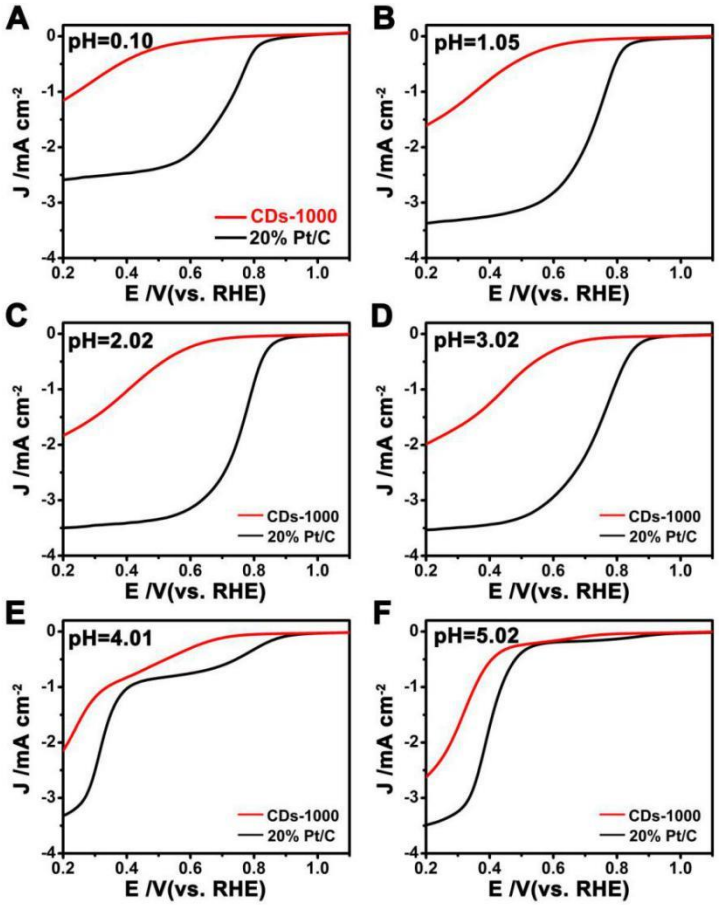

Fig. S12 The ORR polarization plots of CDs-1000 and commercial 20% Pt/C catalyst in pH 0.1 (A), 1.05 (B), 2.02 (C), 3.02 (D), 4.01 (E) and 5.02 (F) electrolytes keeping the [K^+] at 1mol/L (scan rate, 10 mV/s).

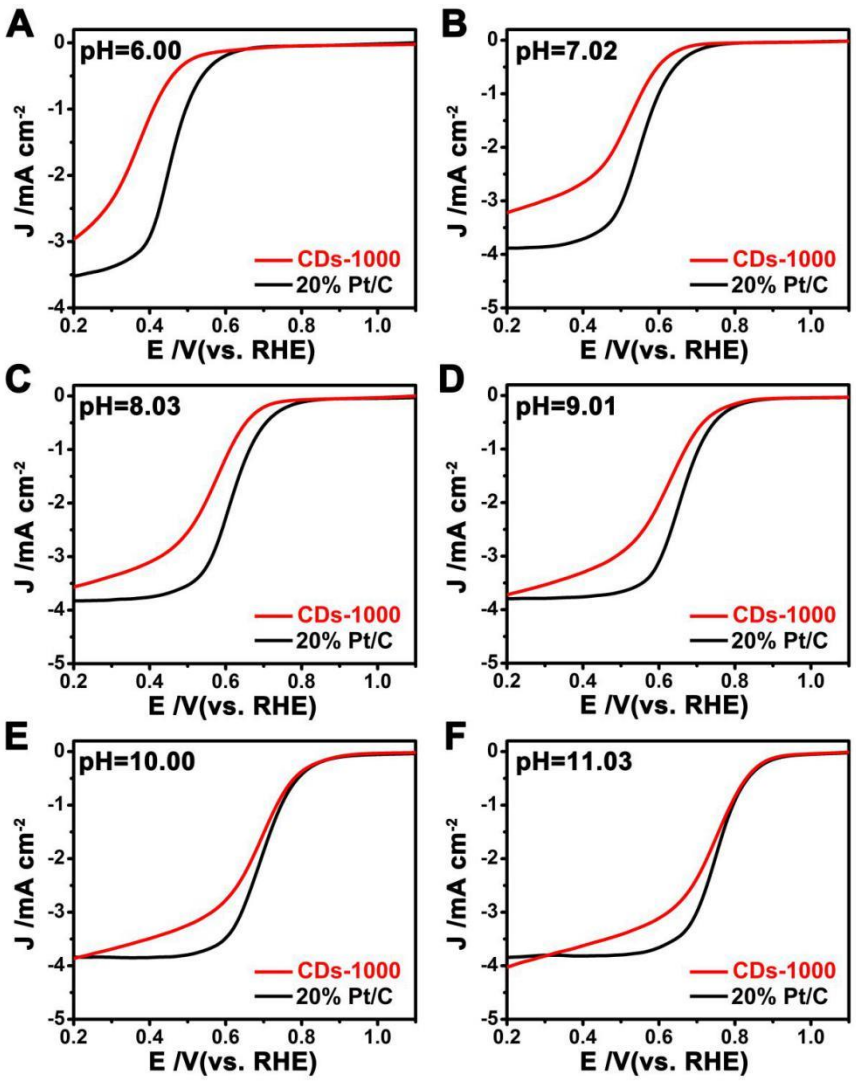

Fig. S13 The ORR polarization plots of CDs-1000 and commercial 20% Pt/C catalyst in pH 6.00 (A), 7.02 (B), 8.03 (C), 9.01 (D), 10.0 (E) and 11.03 (F) electrolytes keeping the [K^+] at 1mol/L (scan rate, 10 mV/s).

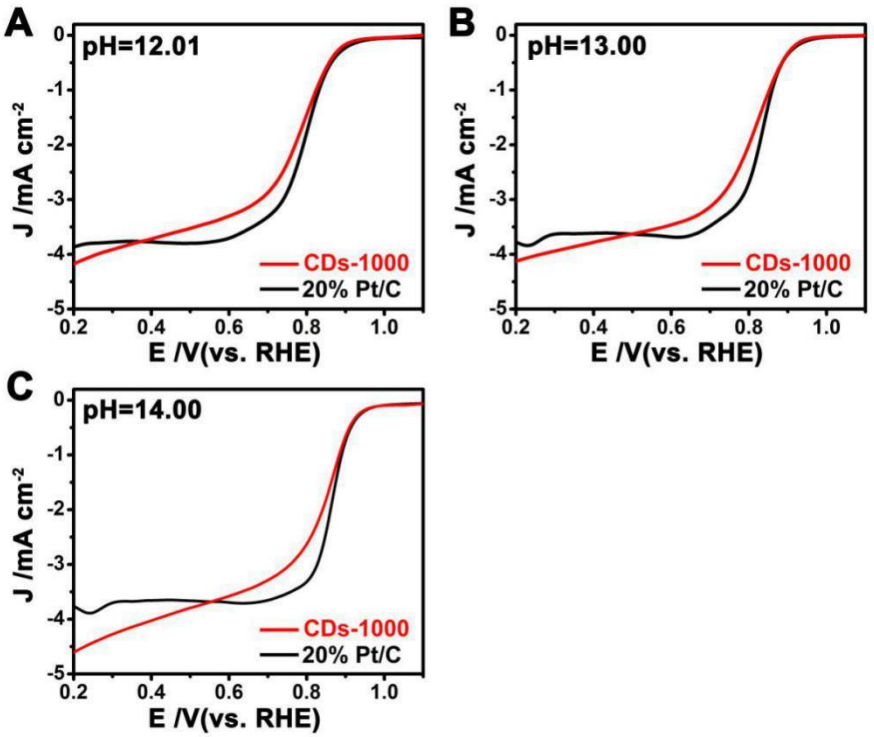

Fig. S14 The ORR polarization plots of CDs-1000 and commercial 20% Pt/C catalyst in pH 12.01 (A), 13.00 (B) and 14.00 (C) electrolytes keeping the [K^+] at 1mol/L (scan rate, 10 mV/s).

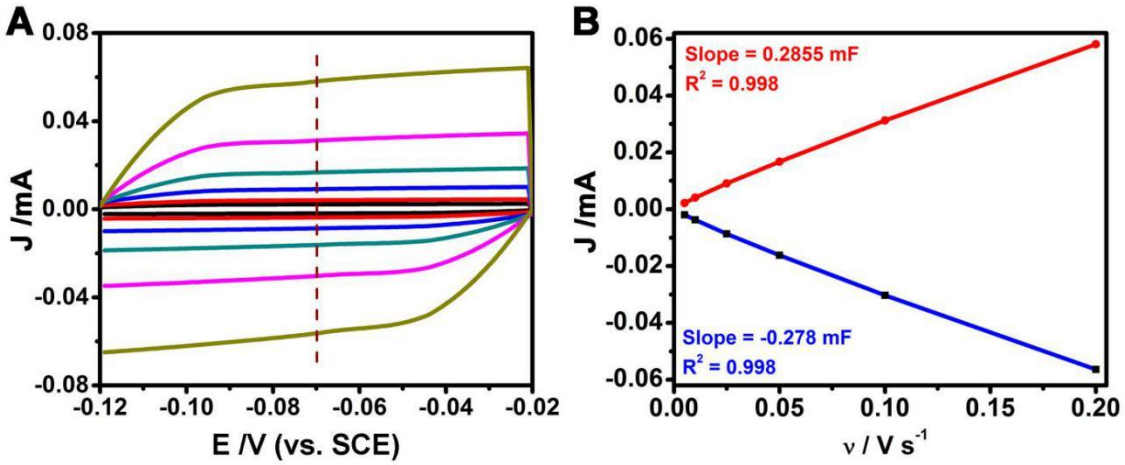

Fig. S15 (A) Cyclic voltammograms were measured in a non-Faradaic region of the voltammogram at the following scan rate: 0.005 (black line), 0.01 (red line), 0.025(blue line), 0.05 (dark cyan line), 0.1 (magenta line), 0.2 (dark yellow line) V/s. The working electrode was held at each potential vertex for 10 s before the beginning the next sweep. All current is assumed to be due to capacitive charging. (B) The cathodic (red open circle) and anodic (blue open square) charging currents measured at -0.07 V vs SCE plotted as a function of scan rate. The determined double-layer capacitance of the system is taken as the average of the absolute value of the slope of the linear fits to the data.

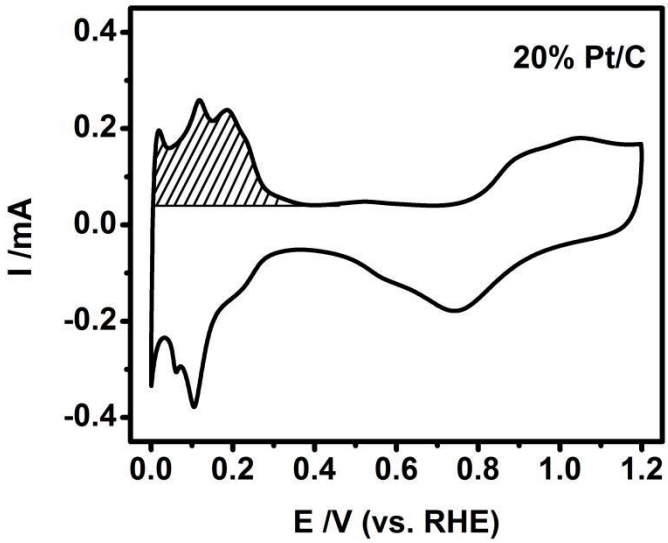

Fig. S16 CV curves of 20%Pt/C. Data was collected at 50mV/s in N_2-saturated 0.1 M $HClO_4$ solution.

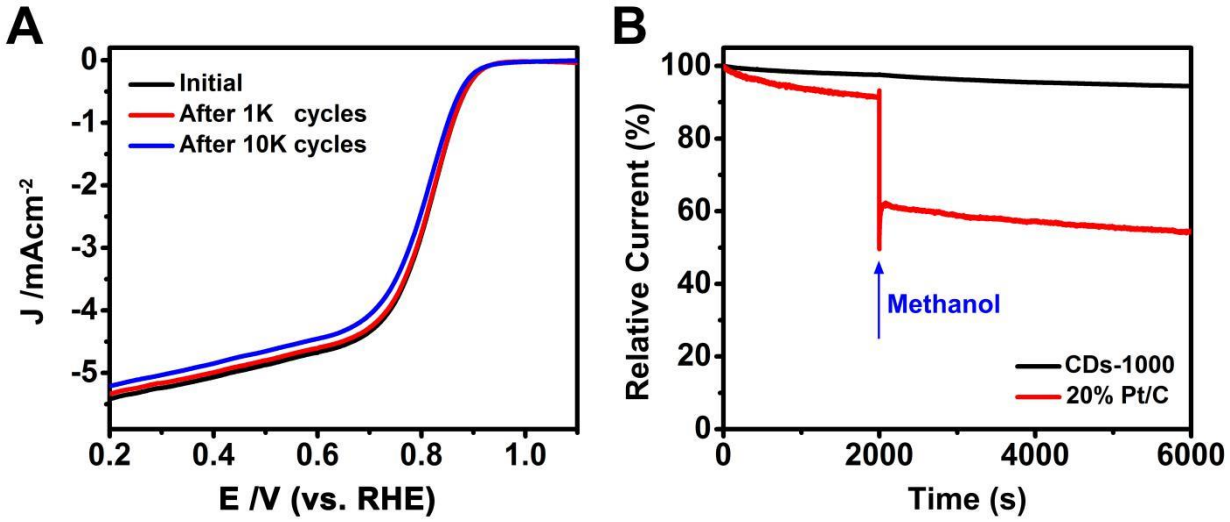

Fig. S17 (A) ORR polarization curves of CDs-1000 catalyst before and after 1,000 cycles, and after 10,000 cycles between 0.6 and 1.1 V (vs. RHE). (B) Chronoamperometric response of CDs-1000 and 20% Pt/C at 0.6 V (vs. RHE) in O_2-saturated 0.1M KOH aqueous solution with addition of 3 M methanol.

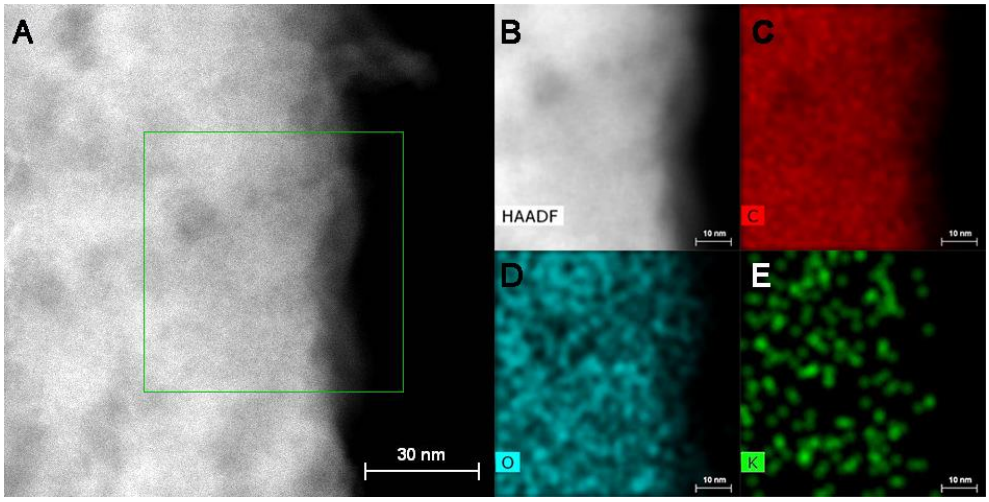

Fig. S18 HAADF - STEM image (A, B), and the corresponding elemental mapping images of CD-K (C:carbon; D:oxygen; E: potassium).

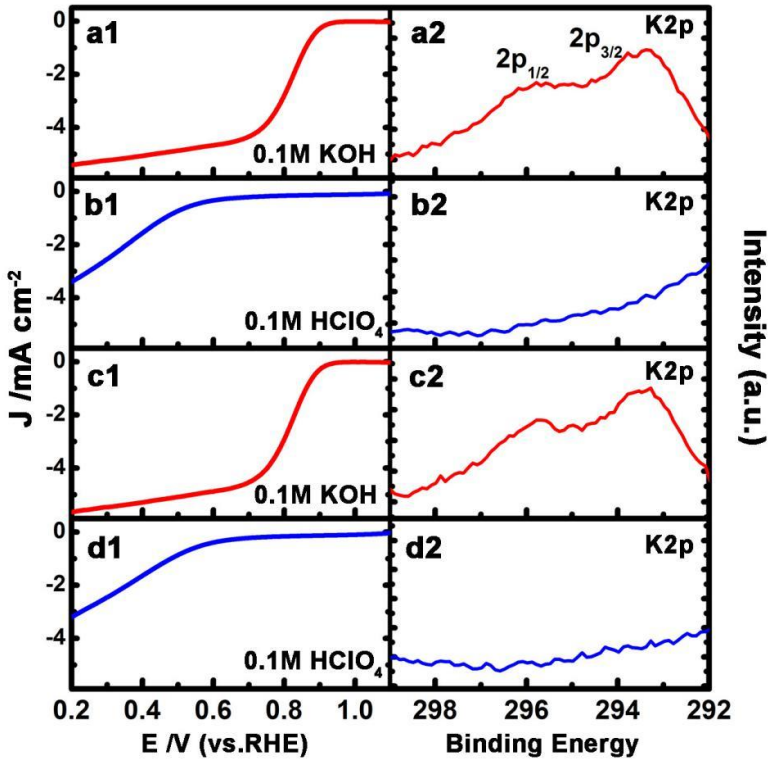

Fig. S19 ORR polarization curves and high-resolution XPS spectra of K2p for CDs-1000 which was tested in alkali and acid solutions cyclically. All solutions were saturated by O_2, Scan rate, 10 mV/s.

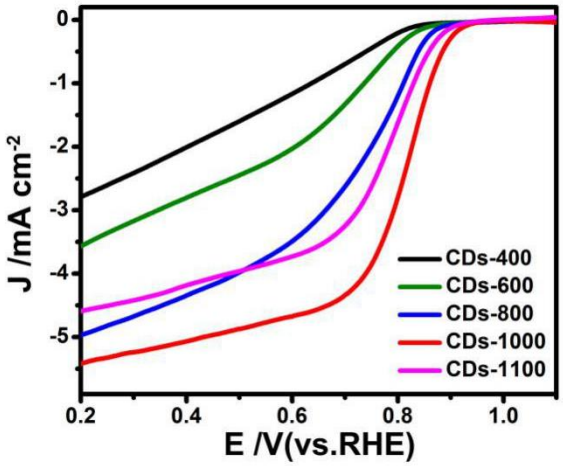

Fig. S20 ORR polarization curves for CDs-400 (black line), CDs-600 (green line), CDs-800 (blue line), CDs-1000 (red line) and CDs-1100 (pink line) catalysts. The Linear scan voltammogram (LSV) curves were recorded at an RDE (1,600 rpm) in an O_2-saturated 0.1 M KOH aqueous solution. Scan rate, 10 mV/s. (mass loading of 0.35 mg/cm^2)

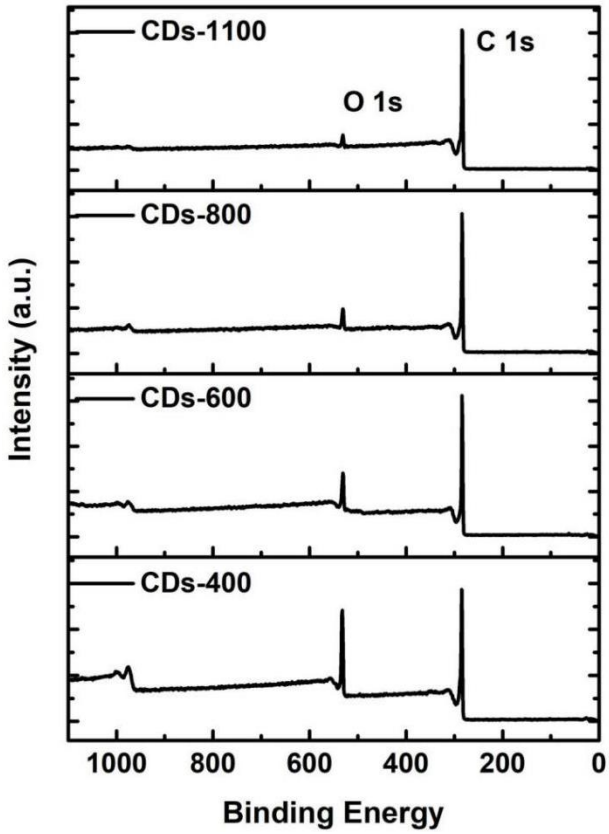

Fig. S21 XPS survey spectra of CDs-400, CDs-600, CDs-800 and CDs-1100. The absence of any other element signal indicates that CDs-temperature prepared from the undoped process are truly undoped, as also confirmed by combustion analyses.

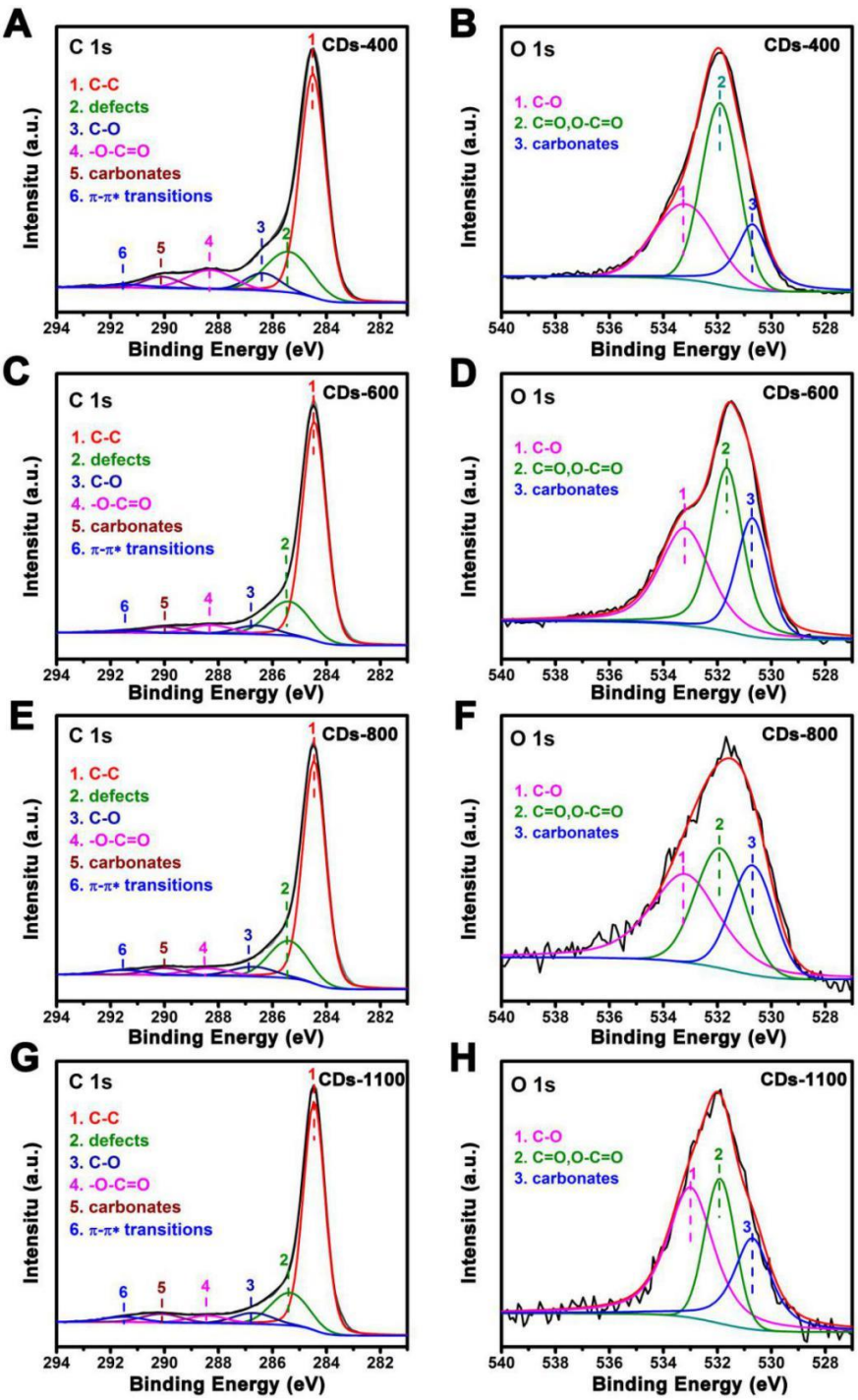

Fig. S22 High-resolution XPS spectra of C1s (A C E G) and O1s (B D F H) for CDs-400, CDs-600, CDs-800 and CDs-1100.

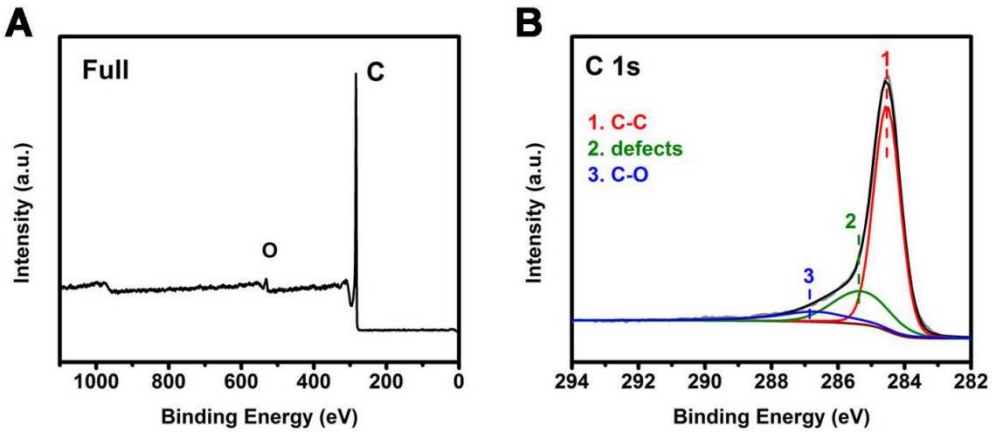

Fig. S23 (A) XPS survey spectrum of Re-CDs-1000. (B) High-resolution XPS spectra of C1s for Re-CDs-1000.

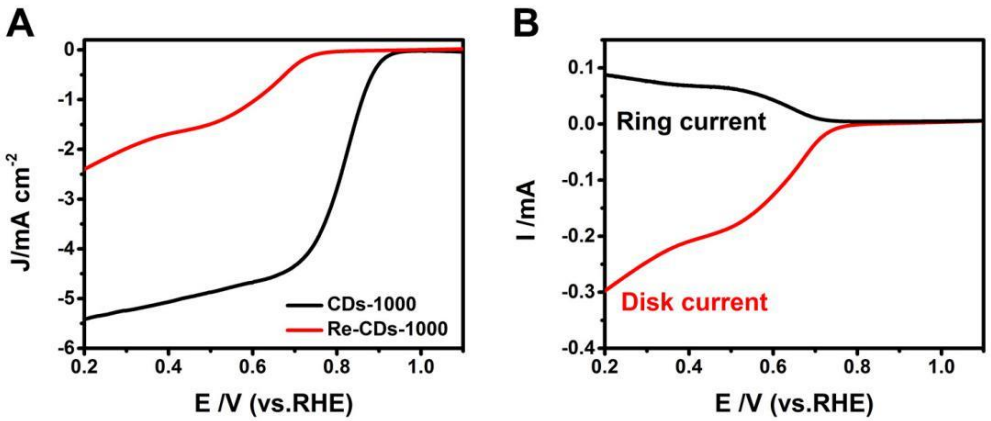

Fig. S24 (A) ORR polarization curves for CDs-1000 (black line) and Re-CDs-1000(red line) catalysts. (B) RRDE LSV curves for Re-CDs-1000 with GC disk-Pt ring electrodes applying a rotating speed of 1,600 rpm in 0.1M KOH (scan rate, 10 mV/s). The Pt ring was biased at 1.5 V versus RHE. The electron transfer number of the Re-CDs-1000 catalyst was calculated to be 2.3-2.6.

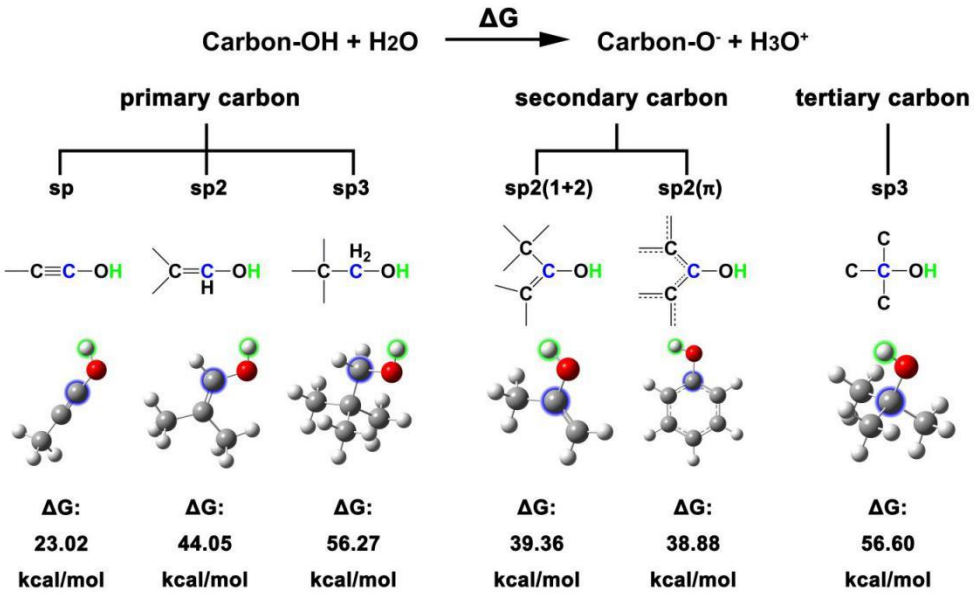

Fig. S25 Models and calculation results for the proton donation capacities connecting hydroxyl groups of different kinds of carbon.

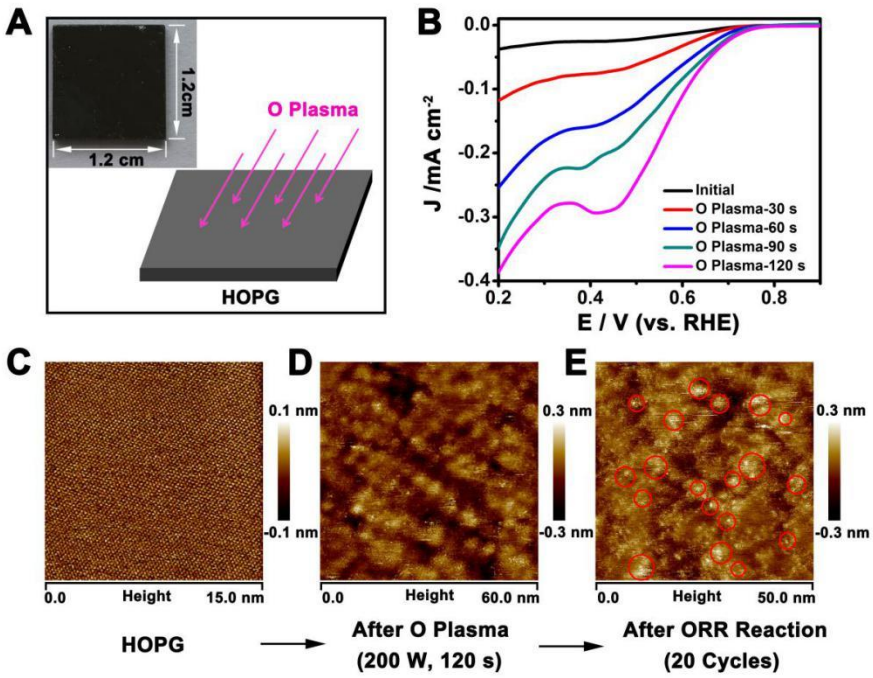

Fig. S26 (A) Schematic diagram of O Plasma treatment on HOPG (1.2 cm * 1.2 cm * 0.2 cm). (B) ORR polarization curves for HOPG (after O Plasma treatment from 30s to 120s; Power: 200 W). The Linear scan voltammogram (LSV) curves were recorded in an O_2-saturated 0.1 M KOH aqueous solution, Scan rate, 10 mV/s. (C) STM image of original HOPG. (D) STM image of HOPG after treatment by O Plasma for 120s. (E) STM image of the HOPG (treated by O-Plasma for 120s) after ORR reaction.

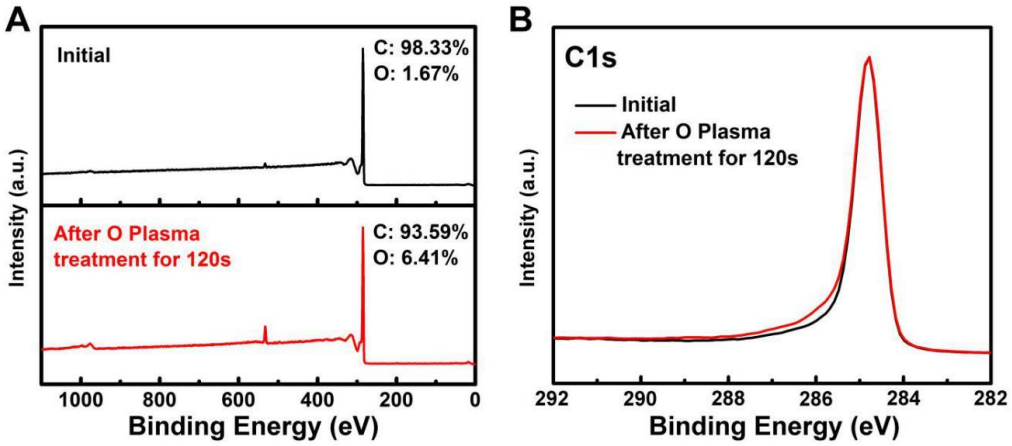

Fig. S27 (A) XPS survey spectra of initial HOPG (black line) and HOPG after O Plasma treatment for 120s (red line). (B) XPS spectra of C1s of initial HOPG (black line) and HOPG after O Plasma treatment for 120s (red line).

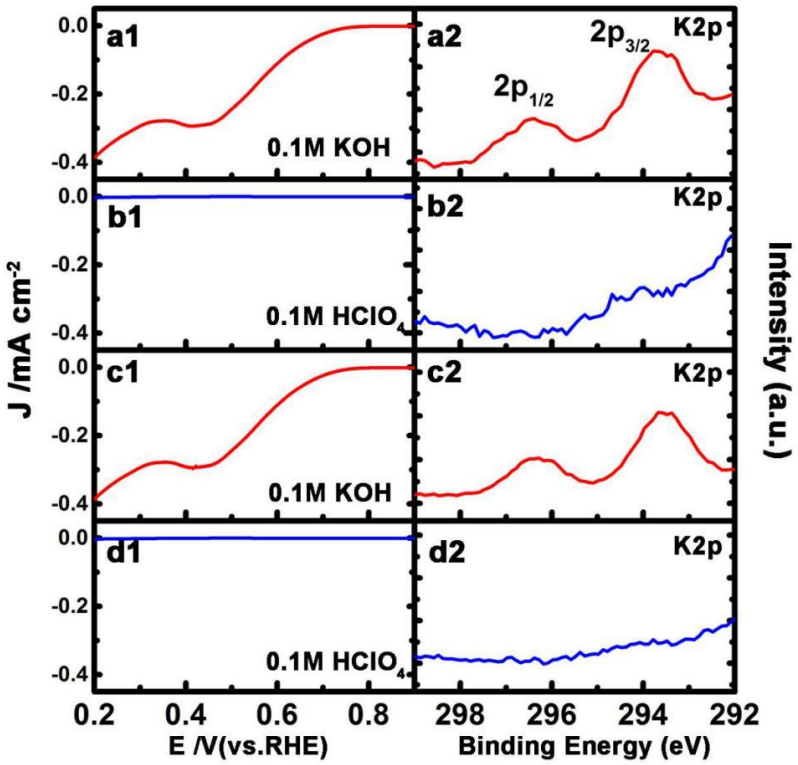

Fig. S28 ORR polarization curves and high-resolution XPS spectra of K2p for HOPG (after O Plasma for 120s), which was tested in alkali and acid cyclically. (a1) the LSV curve was recorded in a 0.1 M KOH aqueous solution first time, (b1) then the LSV curve was recorded in 0.1 M $HClO_4$ aqueous solution. (c1) the LSV curve was recorded in 0.1M KOH second time, (d1) Then the LSV curve was recorded in 0.1M $HClO_4$ second time, (a2, b2, c2,d2) the high-resolution XPS

spectra of K2p for HOPG after ORR and wished, respectively. All solution saturated by O_2, Scan rate, 10 mV/s.

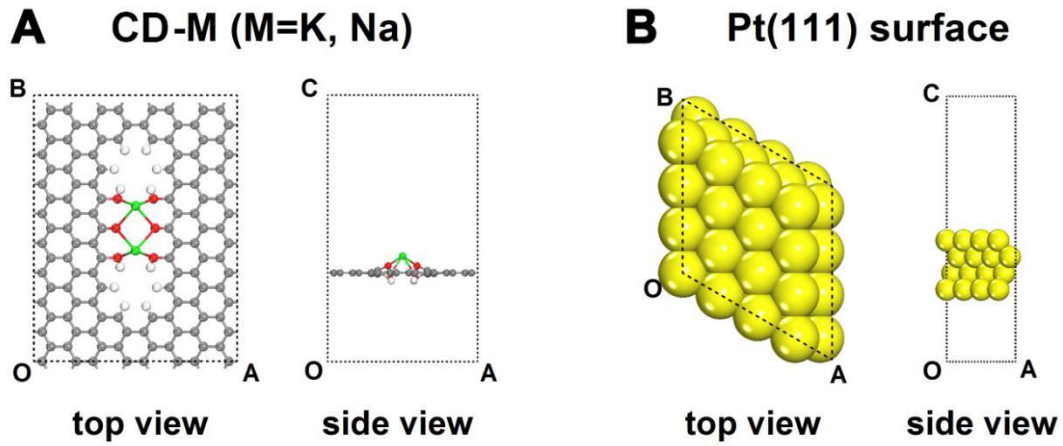

Figure S29 (A). The CD-M models. M represents alkali metal ions (K^+ or Na^+). The gray, white, red and green balls indicate the carbon, hydrogen, oxygen and metal atoms. (B). The Pt (111) surface model. The yellow balls indicate the Pt atoms.

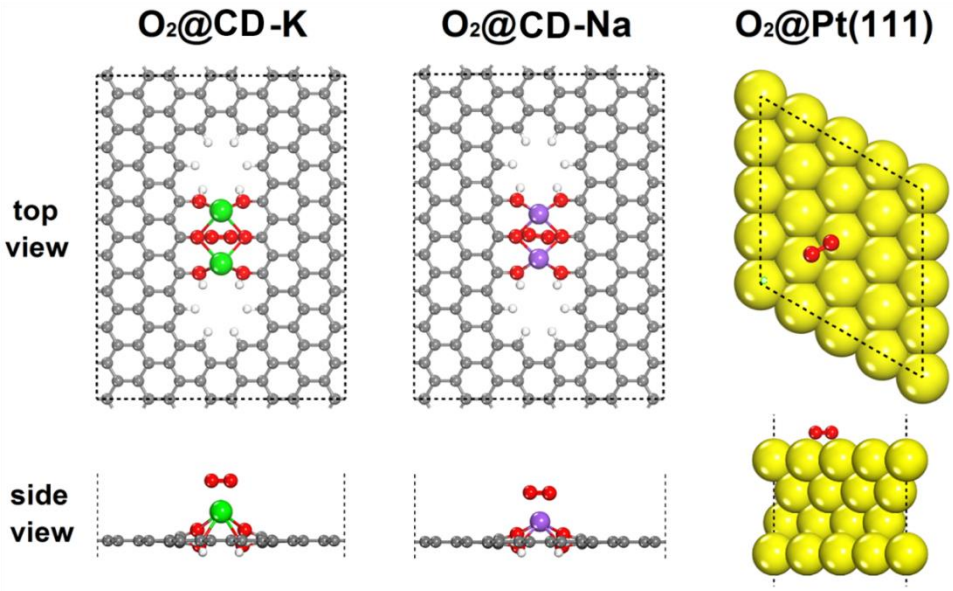

Fig. S30 The optimized geometry structures of O_2@CD-K, O_2@CD-Na and O_2@Pt(111). The gray, red, white, green, purple and yellows balls indicate the C, O, H, K, Na and Pt atoms, respectively.

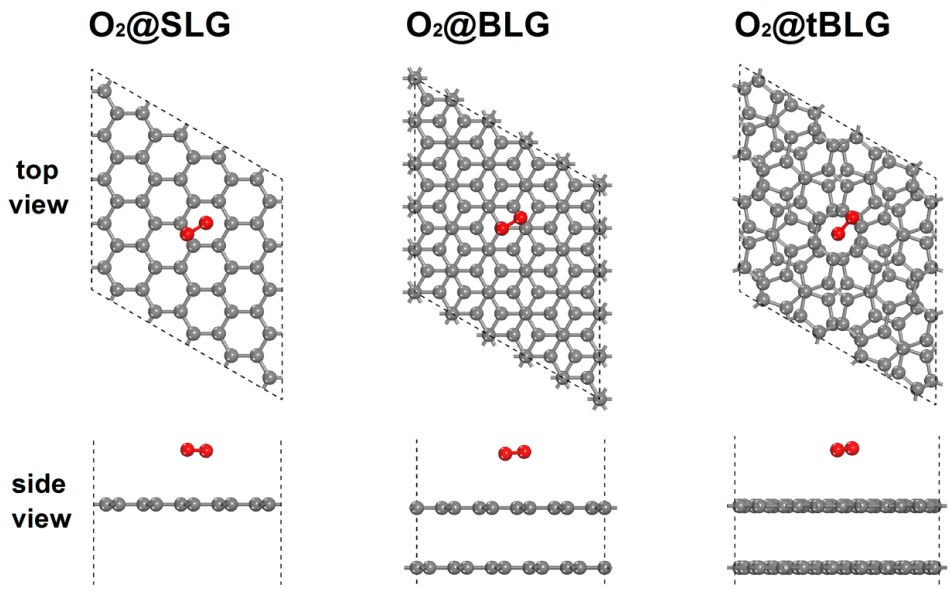

Fig. S31 The optimized geometry structures of O_2@SLG, O_2@BLG and O_2@tBLG. The gray and red balls indicate the C and O atoms, respectively.

3. Tables:

Table S1. Elemental compositions of CDs and CDs-1000. The results come from XPS, elemental analysis and ICP.

	XPS Results (at.%)		**Combustion elemental analysis results (at. %)**			**ICP results (at. %)**										
	C	O	C	H	O	Fe	Co	Ni	Cu	Mn	Al	Na	K	Mg	Ca	Zn
CDs	74.05	25.95	55.30	27.81	16.89	BDL	BDL	BDL	BDL	BDL	BDL	BDL	BDL	BDL	BDL	BDL
CDs-1000	93.64	6.36	89.79	4.95	5.26	BDL	BDL	BDL	BDL	BDL	BDL	BDL	BDL	BDL	BDL	BDL

BDL: below detection limit.

Table S2. The ORR activity of diverse catalysts (V vs RHE) in alkaline media.

Catalysts	E_{oneset}(V)	$E_{1/2}$(V)	J (mA cm^{-2})	n	Reference
CDs-1000	0.960	0.850	5.40	3.90	This work
20% Pt/C	0.970	0.850	5.00	3.90	This work
GSC-900	0.890	0.800	5.34	4.00	22

NLPC	0.920	0.835	5.85	3.91-3.98	23
MZ8-S-P	0.964	0.855	5.89	3.90	24
SN-PC-a	0.912	0.825	5.70	3.90	25
N-PPC-900	0.950	0.816	4.70	~4.00	26
G-BGQD4	0.950	0.800	4.20	3.81	27
P-N-GFs-HMPA	0.980	0.780	4.70	3.93	28
NPGCNs-NaCl	0.962	0.800	4.60	4.00	29
NS-3DrGO-950	0.895	0.732	5.23	3.87	30

Table S3. Elemental compositions of other samples. The results come from XPS, elemental analysis and ICP.

	XPS Results (at.%)		**Combustion elemental analysis results (at. %)**			**ICP results (at. %)**										
	C	O	C	H	O	Fe	Co	Ni	Cu	Mn	Al	Na	K	Mg	Ca	Zn
CDs-400	79.52	20.48	65.55	21.79	12.66	BDL	BDL	BDL	BDL	BDL	BDL	BDL	BDL	BDL	BDL	BDL
CDs-600	87.23	12.77	75.15	14.12	10.73	BDL	BDL	BDL	BDL	BDL	BDL	BDL	BDL	BDL	BDL	BDL
CDs-800	90.31	9.690	83.61	8.75	7.64	BDL	BDL	BDL	BDL	BDL	BDL	BDL	BDL	BDL	BDL	BDL
CDs-1100	96.15	3.85	93.68	3.20	3.12	BDL	BDL	BDL	BDL	BDL	BDL	BDL	BDL	BDL	BDL	BDL
Re-CDs-1000	97.85	2.15	93.12	5.01	1.87	BDL	BDL	BDL	BDL	BDL	BDL	BDL	BDL	BDL	BDL	BDL

BDL: below detection limit.

Table S4. Computational parameter settings in geometry optimizations.

Geometry Optimizations	Spin	SCF Tolerance (Ha)	SCF Smearing (Ha)	k-points	Cutoff (Å)
CD-K	Restricted	1e-5	0.005	2x2x1	5.6
O_2@CD-K	Unrestricted	1e-5	0.005	2x2x1	5.6
O_2 in CD-K box	Unrestricted	1e-5	0.005	2x2x1	3.3
CD-Na	Restricted	1e-5	0.005	2x2x1	5.2
O_2@CD-Na	Unrestricted	1e-5	0.005	2x2x1	5.2
O_2 in CD-Na box	Unrestricted	1e-5	0.005	2x2x1	3.3
Pt(111)	/	/	/	/	/
O_2@Pt(111)	Unrestricted	1e-5	0.005	2x2x1	4.5

O_2 in Pt box	Unrestricted	1e-5	0.005	2x2x1	3.3

Table S5. The optimized geometric parameters of all computational models. The O-O distance represents the bond distance of O_2 molecule. The O-M distance represents the nearest distance between O (belongs to O_2) and metal ion (K^+ or Na^+). The M-M distance indicates the distance between two K^+ or two Na^+.

Systems	O-O distance (Å)	O-M distance (Å)	M-M distance (Å)
CD-K			3.729
O_2@CD-K	1.320	2.877	3.636
O_2 in CD-K box	1.224		
CD-Na			3.180
O_2@CD-Na	1.325	2.530	3.043
O_2 in CD-Na box	1.224		
Pt(111)			2.775
O_2@Pt(111)	1.343	2.122	2.775
O_2 in Pt(111) box	1.224		

Table S6. Computational parameter settings in energy calculations.

Energy Calculation	Spin	SCF Tolerance (Ha)	SCF Smearing (Ha)	k-points	Cutoff (A)
CD-K	Restricted	1e-6	0.0025	9x7x1	5.6
O_2@CD-K	Unrestricted	1e-6	0.0025	9x7x1	5.6
O_2 in CD-K box	Unrestricted	1e-6	0.0025	9x7x1	5.6
CD-Na	Restricted	1e-6	0.0025	9x7x1	5.2
O_2@CD-Na	Unrestricted	1e-6	0.0025	9x7x1	5.2
O_2 in CD-Na box	Unrestricted	1e-6	0.0025	9x7x1	5.2
Pt(111)	Restricted	1e-6	0.003	16x16x1	4.5
O_2@Pt(111)	Unrestricted	1e-6	0.003	16x16x1	4.5
O_2 in Pt box	Unrestricted	1e-6	0.003	16x16x1	4.5

Table S7. Energy calculation results.

Systems	Total DFT-D Energy (Ha)	Adsorption Energy (EA) (kcal/mol)
CD-K	-6304.1908426	
O_2 in CD-K box	-150.2504374	
O_2@CD-K	-6454.4645172	-14.582
CD-Na	-5429.1808868	
O_2 in CD-Na box	-150.2505974	
O_2@CD-Na	-5579.4524573	-13.161

Pt(111)	-12506.0760841	
O_2 in Pt(111) box	-150.2506558	
O_2@Pt(111)	-12656.3482200	-13.479

Table S8. Population analysis results.

Systems	Charge on O Mulliken/Hirshfeld	Net spin on O Mulliken/Hirshfeld	Charge on metal Mulliken/Hirshfeld
CD-K			0.911/0.596
O_2 in CD-K box	0.000/0.00	1.000/1.000	
O_2@CD-K	-0.305/-0.201	0.646/0.631	0.878/0.479
CD-Na			0.860/0.497
O_2 in CD-Na box	0.000/0.000	1.000/1.000	
O_2@C D-Na	-0.305/-0.193	0.631/0.616	0.820/0.390
Pt(111)			-0.034/-0.017
O_2 in Pt(111) box	0.000/0.000	1.000/1.000	
O_2@Pt(111)	-0.118/-0.100	0.344/0.322	0.034/0.062

Table S9. Computational parameter settings in geometry optimizations for O_2@SLG, O_2@BLG and O_2@tBLG.

Geometry Optimizations	Spin	SCF Tolerance (Ha)	SCF Smearing (Ha)	k-points	Cutoff (Å)
O_2@SLG	Unrestricted	1e-5	0.005	2x2x1	3.7
O_2@BLG	Unrestricted	1e-5	0.005	2x2x1	3.7
O_2@tBLG	Unrestricted	1e-5	0.005	2x2x1	3.7

Table S10. DFT optimized geometric parameters of O_2@SLG, O_2@BLG and O_2@tBLG systems. The O-O distance represents the bond distance of O_2 molecule. The O-G distance represents the distances between O atom and the graphene sheet.

Systems	O-O distance (Å)	O-G distance (Å)
Free O_2	1.224	
O_2@SLG	1.240	3.038 / 3.161
O_2@BLG	1.243	3.079 / 3.184
O_2@tBLG	1.242	3.089 / 3.182

Table S11. Computational parameter settings in energy calculations for O_2@SLG, O_2@BLG and O_2@tBLG models.

Energy Calculation	Spin	SCF Tolerance (Ha)	SCF Smearing (Ha)	k-points	Cutoff (A)
O_2@SLG	Unrestricted	1e-6	0.0025	15x15x1	3.7
O_2@BLG	Unrestricted	1e-6	0.0025	15x15x1	3.7
O_2@tBLG	Unrestricted	1e-6	0.0025	15x15x1	3.7

Table S12. The calculated adsorption energies and charge distributions of O_2@SLG, O_2@BLG and O_2@tBLG systems.

Systems	Adsorption energy (EA) (kcal/mol)	Charge on O Mulliken/Hirshfeld
O_2@SLG	-3.12	-0.040 / -0.037
O_2@BLG	-3.25	-0.047 / -0.043
O_2@tBLG	-3.18	-0.044 / -0.041

Reference

1 Y. Liang, H. Wang, J. Zhou, Y. Li, J. Wang, T. Regier and H. Dai, *J. Am. Chem. Soc.*, 2012, **134**, 3517–3523.
2 S. k. Zecevic, J. S. Wainright, M. H. Litt, lj Gojkovic and R. F. Savinell, *J Electrochem Soc*, 1997, **144**, 2973–2982.
3 O. Antoine and R. Durand, *J. Appl. Electrochem.*, 2000, 839–844.
4 G. Gryglewicz, J. Machnikowski, E. Lorenc-Grabowska, G. Lota and E. Frackowiak, *Electrochimica Acta*, 2005, **50**, 1197–1206.
5 S. Trasatti and O. A. Petrii, *Pure Appl Chern*, 1991, **63**, 711–734.
6 J. D. Benck, Z. Chen, L. Y. Kuritzky, A. J. Forman and T. F. Jaramillo, *ACS Catal.*, 2012, **2**, 1916–1923.
7 T. A. Centeno and F. Stoeckli, *J. Power Sources*, 2006, **154**, 314–320.
8 A. D. Becke, *J. Chem. Phys.*, 1993, **98**, 5648–5652.
9 C. Lee, W. Yang and R. G. Parr, *Phys Rev B*, 1988, **37**, 785.
10 W. J. Hehre, R. Ditchfield and J. A. Pople, *J. Chem. Phys.*, 1972, **56**, 2257–2261.
11 S. Grimme, *J. Chem. Phys.*, 2006, **124**, 034108.
12 F. Weigend and R. Ahlrichs, *Phys. Chem. Chem. Phys.*, 2005, **7**, 3297.
13 Y. Zhao, N. E. Schultz and D. G. Truhlar, *J. Chem. Theory Comput.*, 2006, **2**, 364–382.
14 A. V. Marenich, C. J. Cramer and D. G. Truhlar, *J. Phys. Chem. B*, 2009, **113**, 6378–6396.
15 *Gaussian 09*, .
16 B. Delley, *J. Chem. Phys.*, 1990, **92**, 508–517.
17 B. Delley, *J. Chem. Phys.*, 2000, **113**, 7756–7764.
18 J. P. Perdew, K. Burke and M. Ernzerhof, *Phys Rev Lett*, 1996, **77**, 3865.
19 S. Grimme, *J. Comput. Chem.*, 2006, **27**, 1787–1799.
20 A. Klamt and G. Schüürmann, *J Chem Soc Perkin Trans 2*, 1993, 799–805.
21 B. Delley, *Mol. Simul.*, 2006, **32**, 117–123.
22 Z. Ma, K. Wang, Y. Qiu, X. Liu, C. Cao, Y. Feng and P. Hu, *Energy*, 2018, **143**, 43–55.

23 Y. Wang, L. Tao, Z. Xiao, R. Chen, Z. Jiang and S. Wang, *Adv. Funct. Mater.*, 2018, **28**, 1705356.
24 Y. Qian, T. An, K. E. Birgersson, Z. Liu and D. Zhao, *Small*, 2018, 1704169.
25 H. Lin, D. Chen, C. Lu, C. Zhang, F. Qiu, S. Han and X. Zhuang, *Electrochimica Acta*, 2018, **266**, 17–26.
26 X. Lei, M. Wang, Y. Lai, L. Hu, H. Wang, Z. Fang, J. Li and J. Fang, *J. Power Sources*, 2017, **365**, 76–82.
27 T. Van Tam, S. G. Kang, K. F. Babu, E.-S. Oh, S. G. Lee and W. M. Choi, *J. Mater. Chem. A*, 2017, **5**, 10537–10543.
28 C. Li, Z. Chen, A. Kong, Y. Ni, F. Kong and Y. Shan, *J. Mater. Chem. A*, 2018, **6**, 4145–4151.
29 L.-X. Zuo, W.-J. Wang, R.-B. Song, J.-J. Lv, L.-P. Jiang and J.-J. Zhu, *ACS Sustain. Chem. Eng.*, 2017, **5**, 10275–10282.
30 Y. Li, J. Yang, J. Huang, Y. Zhou, K. Xu, N. Zhao and X. Cheng, *Carbon*, 2017, **122**, 237–246.